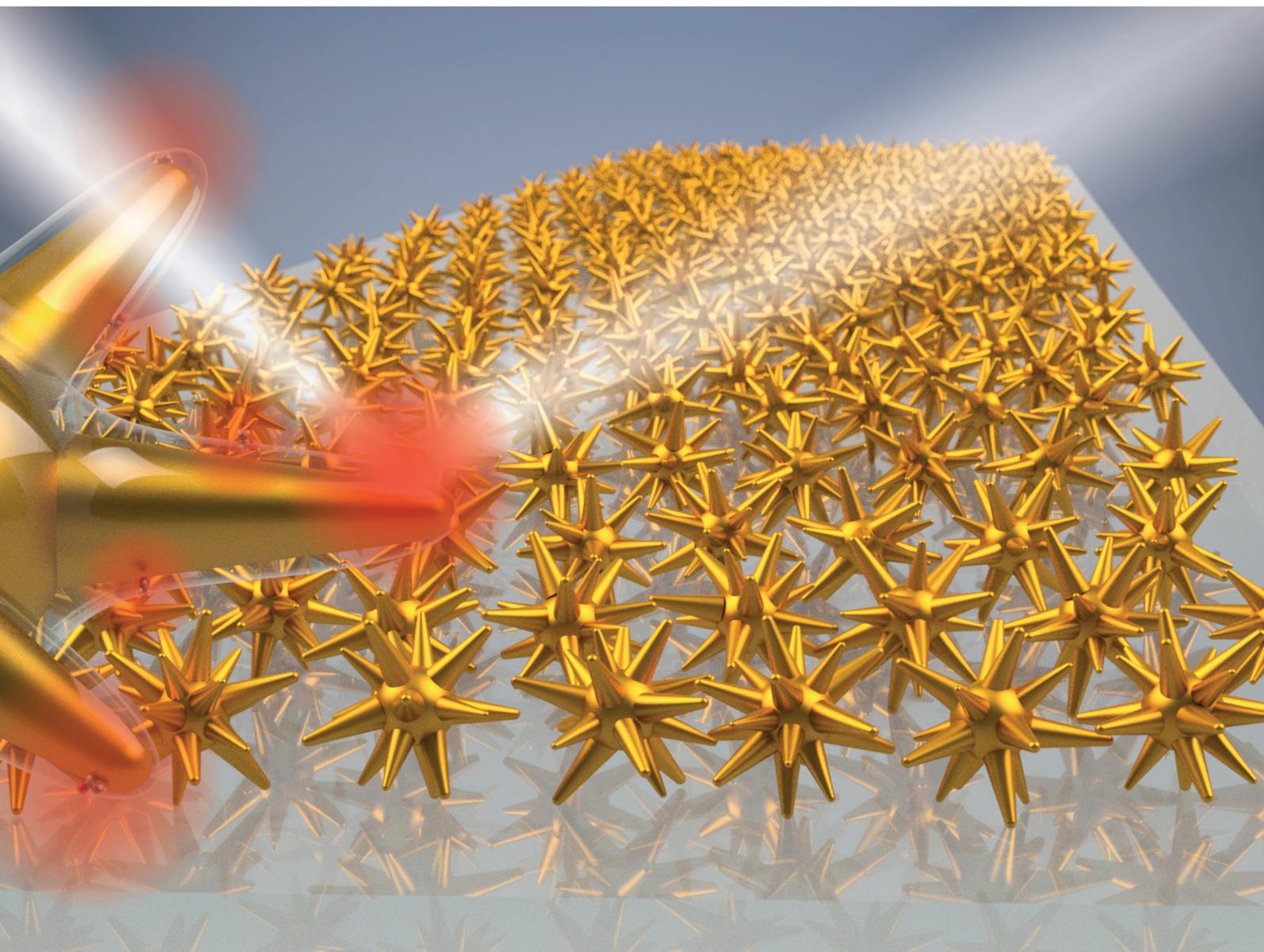# Analyst

ROYAL SOCIETY
OF **CHEMISTRY**

PAPER
Sanda Boca, Cosmin Farcău *et al.*
Self-assembled PVP-gold nanostar films as plasmonic
substrates for surface-enhanced spectroscopies: influence
of the polymeric coating on the enhancement efficiency

Check for updates

Self-assembled PVP-gold nanostar films as plasmonic substrates for surface-enhanced spectroscopies: influence of the polymeric coating on the enhancement efficiency†

Andra-Sorina Tatar,[a] Sanda Boca,*[b,a] Alexandra Falamas,[a] Denisa Cuibus[a] and Cosmin Farcău [ID] *[a]

Colloidal nanoparticles exhibiting anisotropic morphologies are preferred in the structural design of spectroscopically active substrates due to the remarkable optical properties of this type of nano-object. In the particular case of star-like nanoparticles, their sharp tips can act as antennae for capturing and amplifying the incident light, as well as for enhancing the light emitted by nearby fluorophores or the scattering efficiency of Raman active molecules. In the current work, we aimed to implement such star-shaped nanoparticles in the fabrication of nanoparticle films and explore their use as solid plasmonic substrates for surface-enhanced optical spectroscopies. High-density, compact and robust self-assembled gold nanostar films were prepared by directly depositing them from aqueous colloidal suspension on polystyrene plates through convective self-assembly. We investigated the role of the polymeric coating, herein polyvinylpyrrolidone (PVP), in the particle assembly process, the resulting morphology and consequently, the plasmonic response of the obtained films. The efficacy of the plasmonic films as dual-mode surface-enhanced fluorescence (SEF) and surface-enhanced Raman scattering (SERS) substrates was evidenced by testing Nile Blue A (NB) and Rhodamine 800 (Rh800) molecular chromophores under visible (633 nm) *versus* NIR (785 nm) laser excitation. Steady-state and time-resolved fluorescence investigations highlight the fluorescence intensity and fluorescence lifetime modification effects. The experimental results were corroborated with theoretical modelling by finite-difference time-domain (FDTD) simulations. Furthermore, to prove the extended applicability of the proposed substrates in the detection of biologically relevant molecules, we tested their SERS efficiency for sensing metanephrine, a metabolite currently used for the biochemical diagnosis of neuroendocrine tumors, at concentration levels similar to other catecholamine metabolites.

1. Introduction

A great amount of work has been dedicated lately to the design of surface-enhanced spectroscopically active substrates that simultaneously meet the requirements needed for a reliable bioanalytical assay: sensitivity, which translates into the efficiency in signal enhancement; a good limit of detection, which is similar to or exceeds that of clinical laboratory tests; robustness, which is correlated with the capability to provide

reproducible results and withstand certain external influences during the measurement process; low cost and not least, easy preparation.[1–5] With focus on the development of dual-modal platforms for surface enhanced fluorescence (SEF) and surface enhanced Raman scattering (SERS), Lu *et al.* have developed a Ti_6Al_4V bio-metallic substrate with hierarchical structures composed of micro-grooves and nano-ripples that showed enhancement factors of almost 8×10^5 for SERS and over 14 fold for SEF on Crystal Violet used as a model reporter molecule.[6] The proposed system was recently applied for dual-modal detection of blood glucose with 2×10^6 and 25 fold enhancement factors, respectively.[7] Another group demonstrated that triangular wrinkles of a nanostructured Ag film obtained by Ag sputtering on a strained polydimethylsiloxane (PDMS) substrate can act as effective SERS and SEF enhancers for the detection of Crystal Violet and Rhodamine-6G at concentrations as low as 10^{-14} M.[8] Besides the use of patterned films with plasmonic enhancement properties, such effects can also

[a]*National Institute for Research and Development of Isotopic and Molecular Technologies, 67–103 Donat, 400293 Cluj-Napoca, Romania.
E-mail: cfarcau@itim-cj.ro*
[b]*Interdisciplinary Research Institute in Bio-Nano-Sciences, Babes-Bolyai University, 42 Treboniu Laurian, 400271 Cluj-Napoca, Romania.
E-mail: sanda.boca@ubbcluj.ro*

be obtained by growth or by deposition of nanoparticles on substrates. Specifically, through the controlled growth of gold nanoparticles on silicon wafers, the detection of Rhodamine B was achieved *via* SERS and SEF, with a variable output depending on the particle size and density.[9] Silver nanoparticles composed of a silver core, covered in dye molecules and a layer of SiO_2 and further decorated with satellite silver nanoparticles, as probes, were deposited on silanated glass slides and used as SERS-SEF multifunctional substrates with impressive enhancement factors that allow the detection of FITC as low as 10 ppb and 1 ppb *via* SERS and SEF, respectively.[10] Thus, understanding the complex phenomena behind this kind of platform by integrating complementary spectroscopy approaches opens the doors for a plethora of detection applications with improved sensitivity and reproducibility due to the tremendous signal enhancement and the enriched acquired information.

As presented above, one way to easily prepare such SERS or SEF platforms is through the assembly of inorganic nanoparticles such as chemically synthesized gold or silver nanocolloids on solid substrates. Among the various self-assembly strategies, evaporation-induced assembly approaches such as drop-coating, which very often yields circular deposits also known as coffee rings[11,12] and convective self-assembly (CSA), by which films or strip-like deposits can be obtained, represent two of the most commonly used methods.[13] Nanoparticle assembly onto chemically functionalized glass surfaces, which yields randomly distributed colloids and colloidal clusters, represents another alternative.[14] In the continuous expansion of the library of complex plasmonic nanostructures, various molecular ligands such as small molecules, polymers, oligonucleotides or proteins have been used to assist the organization of inorganic nanoparticles into structures of different hierarchical levels. Among the ligands mentioned above, polymers are particularly attractive for nanoparticle assembly due to the complexity of the architectures they enable. By polymer-guided self-assembly, precise control over the nanoparticle location, interparticle interactions and arrangement can be achieved and the resulting nanostructures have functionalities that can be used for a broad range of applications including (bio)sensing, catalysis, energy storage/conversion, electronics and photonics.[15]

Polyvinylpyrrolidone (PVP) is a water soluble polymer of *N*-vinylpyrrolidone used in a multitude of applications, from pharmaceuticals and personal care products, all the way to inks and metallurgy.[16–18] In nanotechnology, it is often used as a coating for nanoparticles, to ensure stability and monodispersity, the interaction with other molecules, or a controlled particle deposition on solid substrates.[19–21]

Gold nanostars (GNSts) are particularly attractive amongst anisotropic nanoparticles due to their shape, many sharp tips and low dips, locations in which, under resonant laser excitation, high electromagnetic fields are generated *via* the lightning-rod effect.[22–24] A lot of work has been focused lately on deciphering the complex plasmonic interactions that take place between GNSts of various aspect ratios and different spike geometries, regarding the detection sensitivity.[25,26] To

exemplify, LSPR-based label-free detection of streptavidin at concentrations as low as 0.1 nM was achieved using biotin-modified gold-nanostars.[27] Also, a detection limit of 1–3 ng ml^{-1} CEA-CAM5 cancer biomarker was achieved by SERS in a gold nanourchin–gold nanourchin sandwich configuration.[28]

Films that are fabricated using different types of nanoparticles assembled as two- or three-dimensional structures have also gained great interest recently.[29] Notably, star-like nanoparticles pre-obtained and further deposited on substrates, or synthesized *in situ* showed remarkable promise in 2D structures. One example is the work of Gummaluri *et al.* in which gold nanourchins have shown improved plasmonic enhancement of light emission by Rhodamine-6G in polyvinyl alcohol (PVA) films, dependent on the particle concentration.[30] Peng *et al.*[31] showed that the trace detection of the miRNA-106a microRNA as a tumour marker was achieved using a SERS sandwich structure that captures the target between Ag/ZnO nanostructures as the substrate and hollow sea-urchin gold nanoparticles as the probe, with a detection limit of 1.84 fmol l^{-1}, verified by RT-qPCR.[31] A SEF immunosensor was developed for the detection of microcystin-LR, using gold nano-crosses deposited electrostatically on a glass substrate, and Cy5 as the fluorescent label. With an appropriate spacer between the fluorophore and particle, a detection limit of 7 pg ml^{-1} was obtained, with enhancement factors of 25–35 fold.[32] Hollow Au/ZnO nanourchins that were directly grown on quartz substrates were demonstrated to function as excellent platforms for SERS sensing of the pesticide thiram at 10 pM, with an enhancement factor of 1.9×10^8.[33] Another example involves the use of ordered monolayers of gold nanourchins that have been synthesized electrochemically directly on thin films. By using this type of platform, the detection of elemental mercury vapours was achieved with a detection limit of 32 μg m^{-3} and astounding accuracy, recovery, precision and increased sensitivity alongside the nanospike size.[34] Another example by Picciolini *et al.*[35] presents a substrate of ZnO tetrapods decorated with branched gold nanoparticles that was used for the apomorphine drug detection with a SERS enhancement factor of up to 7×10^6.[35] Urchin-like ZnO nanoflowers hydrothermally synthesized on a PET substrate and further modified with drop-coated Fe_3O_4 magnetic nanoparticles were used for the development of a novel enzymatic glucose sensor. This complex structure allows non-interfering ultrahigh sensitivity and a wide detection range of glucose, with sustained performance over multiple uses.[36]

In this work, we employed gold nanoparticles with a star-like morphology for the fabrication of compact and robust self-assembled nanoparticle films as surface-enhanced optical spectroscopy active substrates. Besides optimizing the substrate fabrication, we investigated the role of the polymeric coating, herein PVP, in the particle assembly process, the resulting morphology and consequently, the sensitivity of the obtained films. The efficacy of the plasmonic films as SEF or SERS substrates was assessed by the use of Nile Blue A and Rhodamine 800 molecular fluorophores/Raman reporters under visible (633 nm) *versus* NIR (785 nm) laser excitation.

Steady-state and time-resolved fluorescence investigations were performed in order to highlight the fluorescence intensity enhancement and fluorescence lifetime modification effects. The experimental results were corroborated with theoretical modelling by finite-difference time-domain (FDTD) simulations. Furthermore, for proving the extended applicability of the proposed substrates for the detection of biologically relevant molecules, we tested their SERS sensitivity on metanephrine, a metabolite currently used for the biochemical diagnosis of neuroendocrine tumours, at concentration levels similar to those reported for other catecholamine metabolites.

2. Experimental section

2.1 Materials and methods

Hydrogen tetrachloroaurate(III) trihydrate (HAuCl$_4$·3H$_2$O, 99.99%), trisodium citrate, L-ascorbic acid (AA, 99%), poly(vinylpolypyrrolidone) (PVP) of 10 kDa molecular mass, PVP of 55 kDa molecular mass, D,L-metanephrine hydrochloride (C$_{10}$H$_{15}$NO$_3$) 98%-HPLC, Nile Blue and Rhodamine800 were purchased from Sigma-Aldrich. Silver nitrate (AgNO$_3$) was obtained from Merck. Analytical grade ethanol and methanol were used for solubilisation of reporter molecules. Ultrapure water with a resistivity of 18.2 MΩ cm was used for the preparation of aqueous solutions and for rinsing the glassware.

2.2 Synthesis of gold nanostars and conjugation with PVP

Star-like gold nanoparticles were synthesized using a two-step method adapted from the work of Yuan *et al.*[23,37] In the first step, monodisperse 20 nm spherical gold nanoparticles were obtained based on the reduction of an Au(III) precursor with sodium citrate in aqueous solution near the boiling point (the classical citrate method) and further used as seeds or nucleation points.[38,39] In the second step, gold ions (Au^{3+}) from a hydrogen tetrachloroaurate trihydrate (HAuCl$_4$) solution were reduced by ascorbic acid (AA) leading to the growth of spikes from the nanoparticle seeds. It is worth mentioning that the density and the length of the spikes are based on a controlled process influenced by the presence of silver ions (Ag$^-$) in the reaction mixture, which adsorb on certain crystallographic facets, allowing gold deposition at specific selected sites.[23] For particle conjugation with PVP, the polymer was added to the colloidal solution at a concentration that assured full coverage of nanoparticle surface, mixed under continuous stirring at RT, and further purified by centrifugation and resuspension in ultrapure water.

2.3 NP film preparation

Polystyrene plates cut into 10 mm × 25 mm pieces were used as substrates for the preparation of colloidal GNSt assemblies. The plates were cleaned in methanol and isopropyl alcohol, then rinsed in bi-distilled water, followed by nitrogen blow drying. The clean plates were then treated for 20 min in an Ossila UV-ozone cleaning system. This protocol yields clean and hydrophilic surfaces. The treated plates were then used as

support for convective self-assembly. GNSts were purified and highly concentrated, in order to improve the results of the assembly process. A clean glass slide (deposition plate) was placed in an oblique position (at an angle of 15°) with respect to the horizontal substrate plate, which was fixed on a motorized translation stage. A 10 μl drop of GNSts colloid was pipetted into the v-shaped groove formed between the substrate and the deposition plate. The drop is held in position by capillary forces, and a straight meniscus was thus formed on the substrate. Water is evaporated under ambient laboratory conditions, while the substrate is translated at an adequate speed, resulting in the growth of nanoparticle films on the substrate.

2.4 Characterization methods

UV–Vis–NIR optical extinction spectra of colloidal nanoparticles were acquired using a Jasco V-670 spectrometer at 1 nm spectral resolution, in the 200–900 nm spectral range, using 2 mm path length quartz cuvettes. Particle size distribution by dynamic light scattering and zeta-potential were measured using a Zetasizer NanoZS90 instrument from Malvern Instruments, and the analysis was performed at a scattering angle of 90° and temperature of 25 °C. The spectra were measured in triplicate and the median values were calculated. Scanning electron microscopy (SEM) images of gold nanoparticle films were obtained using a Hitachi SU8230 system operating at accelerating voltage of up to 30 kV and magnifications of up to 150 000×. Transmission electron microscopy (TEM) micrographs of colloidal gold nanostars in solution were obtained using a JEOL model JEM1010 microscope, JEOL Ltd, Japan.

2.5 Raman/SERS

Raman/SERS spectra of reporter molecules (NB, Rh800, 10^{-5} M in ethanol) adsorbed onto various substrates (clean polystyrene plate, films of uncoated GNSts, films of PVP-coated GNSts (GNStsPVP)) were acquired using a WITec alpha300 Raman microscope equipped with 633 and 785 nm excitation lasers. SERS spectra were recorded with an integration time of 10 s, an incident power of 2 μW (at 633 nm)/0.3 mW (at 785 nm), a 50× magnification objective, and a 100 μm diameter confocal pinhole. Raman/SERS spectra of metanephrine under 785 nm laser excitation were obtained using the same Raman microscope. A Rh800 10^{-2} M solution was used as the reference for EF calculations.

2.6 Time-resolved fluorescence

Time-correlated single photon counting (TCSPC) investigations were performed using the Chimera (Light Conversion, Lithuania) setup adapted for thin film measurements. The samples were excited at 610 nm using a pulsed laser of 170 fs pulse duration and 80 kHz pulse repetition frequency (Yb: KGW, Pharos, Light Conversion). The 610 nm pump was obtained using an optical parametric amplifier (Orpheus, Light Conversion) from the initial 1030 nm laser beam. The average power of the pump beam was 5 mW at the sample, vertically polarized. A dichroic filter was used to cut the excitation

pump and reflect the fluorescence signal to the monochromator. The emission signal was recorded in the 650–720 nm spectral range with a 2 nm step size. The integration time of the signal was 30 s. The data were analyzed using EasyTau2 software (PicoQuant, Germany) by applying both the reconvolution and the tail-fitting methods. The first one employs the instrument response function (IRF), which was acquired on the day of the experiment using the substrate on which the nanoparticles were deposited, and performs a convolution of the kinetic traces recorded with the measured IRF. The second one fits the decay of the kinetic curves using exponential functions and the beginning of the signal following the incident laser pulse needs to be decided by the user.

2.7 FDTD simulations

Computer simulations of the electromagnetic response were performed using an FDTD algorithm (FDTD module in Ansys-Lumerical). GNSt models were designed in a way to mimic as closely as possible the real structure observed experimentally. Thus, GNSts were constructed from a 60 nm spherical core surrounded by a number of 12 conical spikes (40 nm long, 40° cone angle, 3 nm tip radius) randomly distributed around the sphere. GNSts are either immersed in water (refractive index 1.33) or on a dielectric substrate (refractive index 1.00). To model films, a number of 28 GNSts were arranged on the substrate. Additional modelling was performed on single particles, and ensembles of two, three, or four aligned GNSts. The optical constants of gold are that of Johnson and Chrysty, as provided by the software's database. A rectangular simulation volume of $1 \times 1 \times 1\ \mu m^3$ was considered, with the auto non-uniform mesh type (accuracy level 6), 'conformal variant 0' mesh refinement, and perfectly matched layers on all the sides. An additional mesh with a grid size of 1.5 nm has been added to the region surrounding the particles and the monitors. By using the total-field/scattered-field (TFSF) method the scattering and absorption cross sections of particles excited by a plane wave were calculated. Briefly, a TFSF-type source injects light along the Z direction, polarized either along the X or the Y direction. The absorption cross-section was computed by monitoring the power flowing in/out of a box formed by six monitors, placed inside the TFSF source, and surrounding the particles. The scattering cross-section was measured by a second box monitor placed outside of the TFSF source.

3. Results and discussion

3.1 Characterisation of colloidal nanoparticles

Based on the hypothesis that a polymeric coating might increase particle stability and hence facilitate further manipulation for improving the quality of the nanoparticle films, we conjugated the pristine GNSts with PVP, a polymer that was proven to readily stabilize newly formed nanoparticles by the adsorption of PVP chains onto their surfaces *via* attractive ionic-dipole interactions.[40] The localized surface plasmon resonance (LSPR) band of GNStsPVP in colloidal solution is situated at 733 nm as
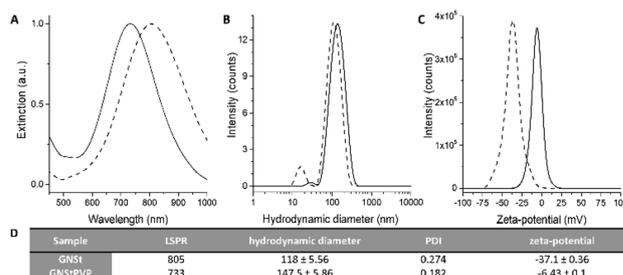

Fig. 1 (A) UV-Vis-NIR extinction spectra, (B) hydrodynamic diameters determined by dynamic light scattering measurements, and (C) zeta-potential of colloidal GNSts (dashed line) and GNStsPVP (full line). (D) Table summarizing the physicochemical characteristics of the colloidal suspensions.

Sample	LSPR	hydrodynamic diameter	PDI	zeta-potential
GNSt	805	118 ± 5.56	0.274	-37.1 ± 0.36
GNStPVP	733	147.5 ± 5.86	0.182	-6.43 ± 0.1

recorded by UV-Vis-NIR extinction spectroscopy (Fig. 1A and D). The obtained nanoparticles are highly monodisperse, having a hydrodynamic diameter of about 150 nm and a zeta-potential of a slightly negative value (−6 mV), as conferred by the PVP polymeric coating (Fig. 1B–D). Transmission electron microscopy (TEM) micrographs in Fig. 2F corroborate with the DLS size values and further show that the GNSts are well-defined, exhibiting large and sharp tips.

3.2 Morphological characterization of nanoparticle films

For the fabrication of nanoparticle films, both uncoated and PVP-coated nanoparticles were deposited onto previously cleaned polystyrene plates using the CSA method. This approach, which was previously employed on other kinds of metal nanoparticles,[41] allows for the direct deposition of the
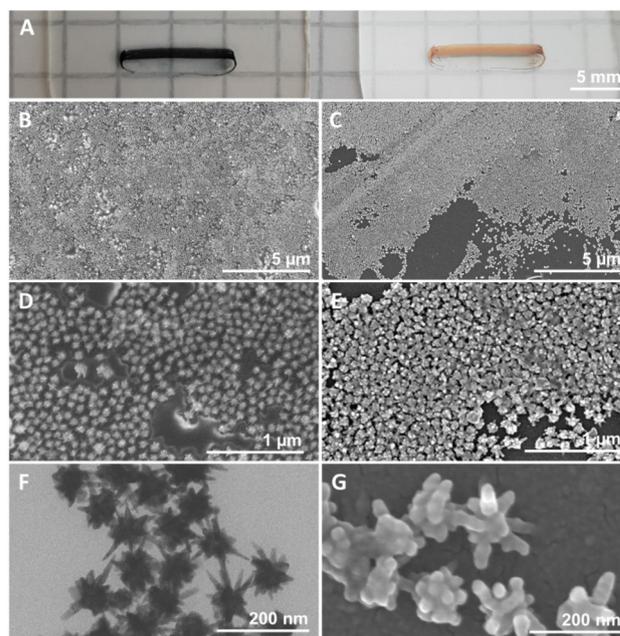
Fig. 2 (A) Photographs of GNStsPVP films obtained in diffuse (left) and specular (right) lighting. (B and D) SEM and (F) TEM micrographs of GNStsPVP films. (C, E and G) SEM micrographs of GNSts.

GNSts from suspension onto various kinds of substrates. By adjusting the dimensions of the substrate and deposition plate, the area covered by the self-assembled films can be adjusted freely. For the purpose of this work, films with a rectangular shape were prepared, sized 1–2 mm × 10–12 mm, as can be observed in the photographs presented in Fig. 2A. This is an area sufficiently large for use with both microscope-based or portable, probe-based Raman systems. Furthermore, the morphology of the GNSts and GNStsPVP nanoparticle films was characterized by scanning electron microscopy (SEM) and the recorded images are illustrated in Fig. 2B–G.

The obtained nanoparticle films exhibit a monolayer arrangement, with quite dense packing of the particles. The occurrence of surface areas free of particles was, however, more frequent on the GNSt films (Fig. 2C), pointing to the positive impact of the PVP coating on the assembly behaviour. TEM images of the colloidal nanoparticles were also acquired, in order to better resolve the GNS morphology (Fig. 2F). Based on these images, an average core diameter of 58 nm and 38 nm average tip length were estimated. On the other hand, a centre-to-centre average interparticle distance of 96 nm was deduced based on SEM images. By corroborating these determinations from both TEM and SEM data, it can be concluded that the dense packing of GNSts involves a considerable overlap/touching of the sharp tips of neighbouring particles in the film. This type of arrangement generates a multitude of narrow interparticle gaps, which together with the sharp tips/spikes favour the generation of enhanced electromagnetic fields when illuminated.

3.3 Optical response and field enhancement of nanoparticle films

The optical response of the deposited GNSt films was further studied and analyzed with reference to the response of GNSts in a colloidal suspension. FDTD simulations were also performed in order to better understand the observed behaviour. Fig. 3A presents the simulated extinction spectrum of a single GNSts compared to the measured spectra of the colloidal nanoparticles in suspension. By modelling the GNSts (Fig. 3C) using geometrical parameters close to the average ones observed experimentally, a good agreement between experiment and simulation was obtained for the spectral position of the extinction band in the 700–800 nm region. The band in the experimental spectrum is however broader, which is not surprising if one considers the heterogeneities in the size and shape of the GNSts' cores and spikes. Note that although the blueshift of the GNStsPVP relative to bare GNSts might seem unexpected, this is a consequence of the relatively high instability of the nanoparticles in the absence of any stabilizer, which translates in terms of tip etching and a transition in time from anisotropic to spherical, a more energetically favourable shape.[42]

The measured extinction spectra of the GNSt films (Fig. 3B) exhibit a broader band than the single particles, behaviour which was also well captured by the simulations performed on dense particle films (Fig. 3D). By considering a population of interparticle distances and particle orientations, the interparti-
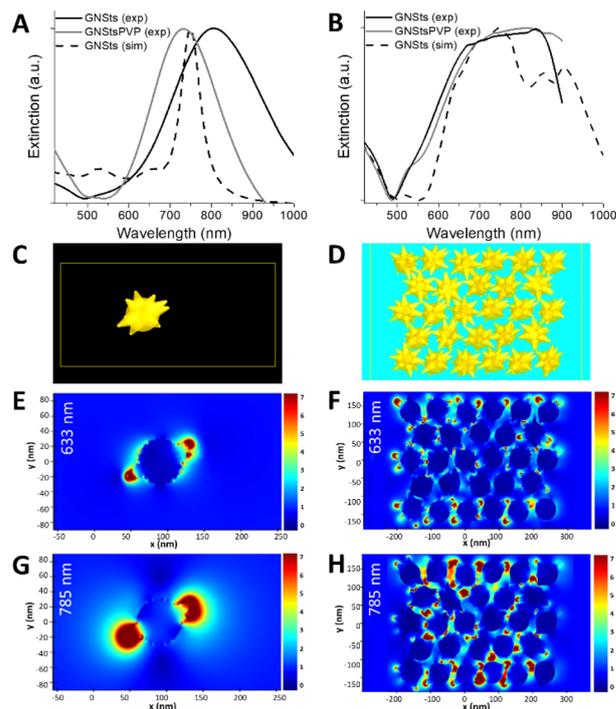
Fig. 3 Experimental extinction spectra of GNSts (black lines) and GNStsPVP (gray lines), and simulated extinction spectra of GNSts (dotted lines) in the colloidal suspension (A) and as films on substrate (B), normalised. Morphology and arrangement used in simulations, modelled for one GNSt in water (C) and for a GNSt film on substrate (D). Calculated electric field magnitudes in the XY plane for one GNSt in water (E and G) and for a GNSts film on substrate (F and H), at 633 nm excitation (E and F) and at 785 nm excitation (G and H).

cle interactions exhibit a broad spectrum and determine the observed optical response. Since a very good correlation between the experiment and simulation was obtained, information concerning the electric fields around the particles can also be extracted and analyzed with confidence. The electric fields are analyzed at 633 nm and 785 nm, two among the most common lasers used on commercially available Raman systems. For the single GNSt case, the enhanced electric fields are mostly located near the apexes of the spikes for both wavelengths (Fig. 3E and G), while the field magnitude is higher at 785 nm, this wavelength being closer to the extinction band maximum. The electric field distribution in the GNSts film is more complex. At 633 nm (Fig. 3F), the location of the enhanced electric fields is similar to the single particle case, near the spikes' apexes, indicating that the interaction between neighbouring particles is weak. At 785 nm (Fig. 3H), on the other hand, electric fields are more intense, and are extending more into the space between the particles, indicating a stronger interparticle coupling. This is even more obvious by analyzing the electric field X and Y components (Fig. S1 in the ESI†). From the practical standpoint, it could mean that enhanced electric fields extend over a larger part of the GNSts, which translates to a higher number of molecules experiencing these large fields, leading to a positive impact on SERS signals.

3.4 Surface-enhanced Raman/fluorescence evaluation

The surface enhanced sensitivity of the GNSts-PVP self-assembled substrates was first investigated by employing test analytes, Nile Blue and Rhodamine800, two chromophores with demonstrated Raman activity, high photo-stability and large quantum yield (see Fig S2 in the ESI† for their absorption and emission spectra). The spectra of the two analytes in the presence and absence of GNSts obtained using 633 and 785 nm excitation are shown in Fig. 4. The results demonstrate that when the samples decorated with NB were excited on-resonance (relative to the fluorophore absorption) at 633 nm, all samples exhibited both fluorescence and SERS signals, which overlapped.

The intensity of the fluorescence emission of NB decreased to similar intensities in the presence of both GNSts and GNStsPVP samples (Fig. 4A). A slightly higher intensity was detected for the GNStsPVP-NB sample in the red spectral region of the signal compared to GNSts-NB. The emission maximum of NB presented a blue-shift in the presence of GNSts from 671 nm to 665 nm, which was not observed in the case of PVP stabilized GNSts. The calculated full-width-at-half-maximum (FWHM) increased from 1106 cm^{-1} for the NB sample to 1172 cm^{-1} in the case of GNSts-NB and to 1367 cm^{-1} in the case of GNStsPVP-NB, suggesting that the PVP layer induced a broadening of the NB emission signal. Also, the integrated area below the emission spectrum was higher for the GNStsPVP samples compared to simple GNSts. Both NB decorated GNSt samples presented the Raman fingerprint band of NB at 590 cm^{-1}, however, in the case of GNStsPVP-NB, a clear improvement in the signal-to-noise ratio was observed. We can conclude that both GNSt samples

induced similar quenching of the fluorescence signal characteristic of NB. Interestingly, NB can be detected based on its SERS fingerprint band even at on-resonance excitation, despite its strong fluorescence and despite the polymeric coating on the GNSts.

At 785 nm off-resonance excitation (relative to fluorophore absorption), the situation differs and only the SERS signal of NB could be recorded in the presence of GNSts (Fig. 4B). In the absence of GNSts, however, the Raman spectrum of NB alone could not be recorded at the concentration and experimental conditions tested in this study. When adsorbed directly onto the GNSts, weak enhancement of NB specific Raman bands was observed, the spectrum presents mainly the 590 cm^{-1} fingerprint band characteristic of NB, assigned to C–C–C and C–N–C deformation vibrations.[43] Additionally, several weak bands located at 495, 662, 1134, 1354, and 1640 cm^{-1} were identified. It is interesting to observe that the PVP stabilized GNSts stimulated higher SERS enhancement compared to bare GNSts, when in fact it could have been expected that the PVP layer would hinder the acquisition of the Raman spectrum. The spectrum collected from the GNStsPVP-NB sample shows a strong intensity fingerprint band at 590 cm^{-1}, together with several medium-to-strong intensity bands located at 495, 547, 662, 1134, 1190, 1354, 1417, 1490, and 1639 cm^{-1}. The integrated area calculated for the 590 cm^{-1} band was 11 times higher in the case of GNSt PVP compared to the bare GNSts, probably due to the sharper tips of the GNSt PVP.

In the case of Rh800, under 633 nm excitation, the fluorescence emission signal presented a maximum at 713 nm (Fig. 4C). The intensity of the signal decreased for both GNSt samples decorated with the fluorophore, however, weaker quenching was detected for the PVP stabilized GNSts. Additionally, a 5 nm blue-shifting of the emission maximum was identified for the GNSts-Rh800 and approximately 2 nm red-shifting for the GNStsPVP-Rh800 sample. A broadening of the fluorescence emission signal characteristic of Rh800 was detected in the presence of the GNStsPVP, as well as increased intensity (integrated band area), similar to the case of NB. The GNStsPVP samples induced weaker quenching of the fluorescence emission signal compared to the bare GNSts for both fluorophores, indicating that GNStsPVP could potentially act as efficient SEF substrates. Moreover, the observation that the fluorescence signal of Rh800 is more than three times higher in the presence of GNStsPVP compared to the uncoated GNSts, while in the case of NB, the emission intensity was similar for both GNSts samples, indicates that GNStsPVP would be more appropriate as SEF substrates for far red-emitting fluorophores.

When the samples were excited off-resonance at 785 nm, both GNSts samples, polymer-coated and uncoated, exhibited the SERS signal of Rh800 (Fig. 4D). When the fluorophore was directly adsorbed onto the GNSts surface, a weak Raman enhancement was obtained. However, the fingerprint bands characteristic of Rh800, located at 470, 1190, 1349, 1437, 1496, and 1645 cm^{-1} could be easily identified. In the presence of
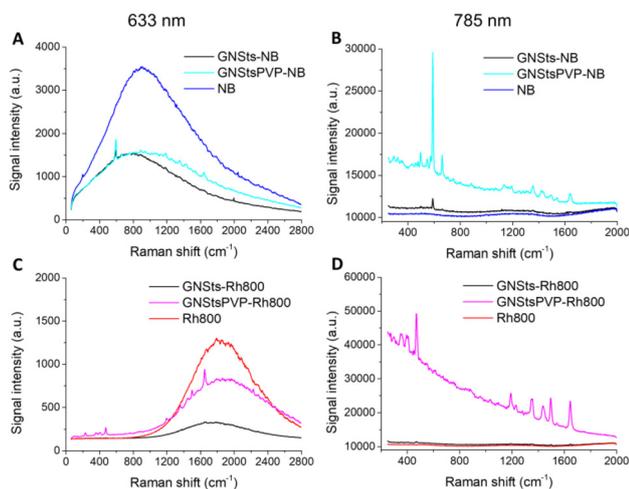
Fig. 4 SERS/fluorescence spectra of (A) NB on GNSts films, NB on GNStsPVP films, and free NB molecules on plastic slides under 633 nm laser excitation; (B) NB on GNSts films, NB on GNStsPVP films, and free NB molecules on plastic slides under 785 nm laser excitation; (C) Rh800 on GNSts films, Rh800 on GNStsPVP films, and free Rh800 molecules on plastic slides under 633 nm laser excitation; (D) Rh800 on GNSts films, Rh800 on GNStsPVP films, and free Rh800 molecules on plastic slides under 785 nm laser excitation.

GNStsPVP, a strong enhancement of the Raman signal specific to Rh800 was detected. Besides the main fingerprint bands, lower intensity peaks were also identified. Signal amplification in the presence of the PVP stabilized GNSts was approximately 32 times higher compared to the uncoated GNSts, as calculated for the 470 cm^{-1} band. An enhancement factor was also calculated based on the SERS spectrum of Rh800 on the GNStsPVP film, and a value of around 3.2×10^5 was obtained. The much stronger Raman amplification compared to the NB case, suggests once more that the enhancement effect of GNSts strongly depends on the fluorophore type. It is important to note that the tested fluorophores were detected based on their SERS fingerprint bands, even at on-resonance excitation, and despite the strong fluorescence or the PVP coating. Further research is necessary in order to elucidate the dimension of the PVP layer needed to appropriately amplify the fluorescence emission signal of the fluorophore,[44] as well as to find out if our GNSts work better with fluorophores emitting in a specific spectral region, or the discussed observations relate to chemical effects.

3.5 Time-resolved fluorescence of GNSt films

Time-resolved fluorescence experiments were further performed to investigate the lifetime of NB in the presence and absence of GNSts. The TCSPC data carpets corresponding to these two sample conditions show the intensity of the fluorescence signal as a function of the emission wavelength and moment of time of photon arrival, and are presented in Fig. 5A and B. The carpets indicate that the intensity of the fluorescence signal is higher in the absence of GNSts than in their presence, suggesting that the same quenching effect as observed before is present.

Additionally, the kinetics of the fluorophore is faster when the molecule is directly adsorbed on the GNSts, which indicates an energy transfer between the fluorophore and the particles. The averaged kinetic traces obtained from all the kinetic traces recorded in the 650–720 nm spectral range are given in Fig. 5C. It is clearly observable that the fluorescence decay kinetics of NB is faster in the presence of GNSts. In order to calculate the lifetime of NB in the presence and absence of GNSts, we fitted the kinetic traces with exponential functions using two methods, the tail-fitting and the reconvolution of the kinetic traces with the IRF. Fig. S3 (ESI†) shows the kinetic

traces recorded at 668 nm in both cases (NB in the presence and absence of GNSts), together with the IRF and the fitted curves obtained using both methods. We observed that the kinetic traces recorded from NB in the absence of GNSts can be well fitted using two exponential functions when the tail-fitting method was used and three exponential functions when the reconvolution method was employed. Even if the fitted curve obtained using two exponential functions gives a satisfactorily fit of the experimental data, the averaged decay time is similar to the one obtained using only one exponential function ($\tau = 1.21 \pm 0.02$ ns). The same is true for the averaged decay time obtained using the reconvolution method, however, the average time decreases drastically compared to the one obtained using the tail-fitting method. This is caused by the time component of less than 100 ps, which is probably obtained due to the residuals resulting from fitting the kinetic curves at early time moments where the excitation laser pulse overlaps with the signal of the sample (Table S1 in the ESI†). In the presence of GNSts, the lifetime of NB decreases drastically, as the recorded kinetic traces are similar to the IRF, meaning that the lifetime of NB could not be resolved anymore and decreased below the resolution of our instrument. The conclusion that can be drawn from these experiments, however, is that in the presence of GNSts the emission signal of NB is quenched, probably due to the energy transfer between the fluorophore and the NPs and thus the lifetime of the fluorophore decreases.

### 3.6 Evaluation of nanoparticle films for bioanalyte detection

As stated above, the efficiency of a substrate to function as a good sensing platform can be measured in not only terms of sensitivity but also in terms of robustness, rapidity, low cost and ease of use or practicability. Moreover, current research on SERS tends to focus on implementing more complex nanoparticles in detection schemes, in order to improve detection sensitivity and to answer the needs of biological analysis rather than building quantitative models that can be used routinely.

Considering these, we have tested the GNStsPVP self-assembled substrates for the rapid detection of metanephrine, a bioanalyte whose SERS-based spectroscopic detection is non-trivial, as suggested by the scarcity of published reports, a possible reason being the poor interaction with noble metal surfaces.[46] The protocol used here implied the dropping of the analyte solution of 10^{-5} M concentration directly onto the nanostructured substrates, followed by the recording of the spectrum under 785 laser excitation. Although they are weakly expressed at this concentration which, however, is comparable to those reported for the SERS sensing of other neurotransmitters on gold nanoparticle substrates (*e.g.* 10^{-4}–10^{-6} M in the case of epinephrine and dopamine),[46,47] the main characteristic peaks of metanephrine were detectable in the 1000–1700 cm^{-1} region (spectrum (a) in Fig. 6 and Table 1): specifically, a band at 1053 cm^{-1} attributed to the $C_{13}O_{12}$ stretching and CH rocking ring, a band at 1145 cm^{-1}, corresponding to the $C_{13}H_{14}H_{15}H_{16}$ twisting, a band at 1200 cm^{-1},
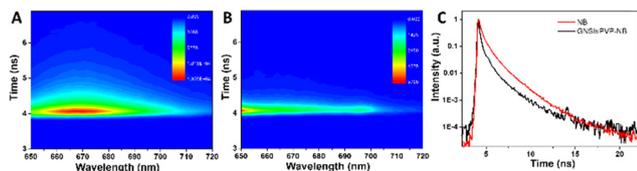
Fig. 5 The TCSPC data carpets corresponding to NB in the absence (A) and the presence (B) of GNSts. The carpets present the intensity of the emission signal as a function of the emission wavelength and moment of time of photon arrival. The averaged kinetic traces (C) characteristic of each sample are also presented.
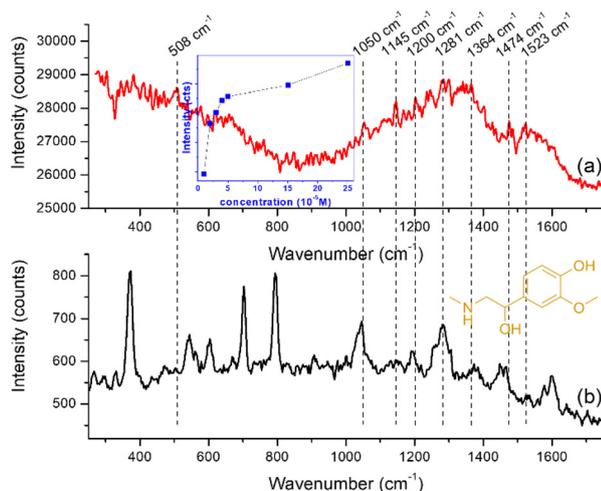
Fig. 6 (a) The SERS spectrum of metanephrine on the GNStsPVP film at 10^{-5} M concentration; dependence of the SERS signal on metanephrine concentration is displayed in the inset. (b) Raman spectrum of metanephrine at 5×10^{-2} M concentration. Both spectra were obtained using 785 nm laser excitation.

Table 1 SERS (a) and Raman (b) band assignment of metanephrine[45]

SERS (cm^{-1})	Raman (cm^{-1})	Band assignment
508	503	Ring out-of-plane deformation
1053	1046	$C_{13}O_{12}$ stretching + CH rocking ring
1145	1145	$C_{13}H_{14}H_{15}H_{16}$ twisting
1200	1193	$O_{18}H_{19}$ deformation + $C_{17}H_{19}$ deformation
1283	1281	CC stretching ring (catechol moiety) + CH rocking ring + C_5O_{10} stretching
1364	1374	$C_{17}H_{19}$ deformation + $C_{20}H_{21}H_{22}$ wagging
1474	1466	$C_{13}H_{14}H_{15}H_{16}$ deformation
1523	1529	CC catechol ring stretching

assigned to the $O_{18}H_{19}$ deformation and $C_{17}H_{19}$ deformation, one at 1283 cm^{-1} assigned to the C–C stretching mode in the catechol moiety, a band at 1364 cm^{-1} resulted from $C_{17}H_{19}$ deformation and $C_{20}H_{21}H_{22}$ wagging, one at 1474 cm^{-1} owing to the $C_{13}H_{14}H_{15}H_{16}$ deformation and finally, one at 1523 cm^{-1} due to the CC catechol ring stretching.[45] For reference, we have considered the normal Raman spectrum of metanephrine in solution at a concentration of 5×10^{-2} M (spectrum (b) in Fig. 6). The dependence of the SERS signal on the metanephrine concentration is displayed in the inset of Fig. 6. Since the linearity is good only on a narrow range, the LOD values obtained by regression analysis are in the range of 1.0×10^{-5} M – 3.1×10^{-4} M, depending on the selection of the range to be analyzed.

Further work is necessary for establishing the selective SERS detection of metanephrine in the presence of other biological components such as glucose, ascorbic acid, or glutamic acid in PBS at normal plasma concentrations. A first step towards this achievement will be to improve the adherence of the GNSts films to their substrate, in order to improve their mechanical stability in aqueous environments.

4. Conclusions

In this study, we demonstrated the fabrication of high-density, compact self-assembled gold nanostar films by direct deposition from aqueous colloidal suspension on solid plates through convective self-assembly. The optical response of these films exhibits a broad extinction band due to interparticle plasmon coupling, making them appropriate for excitation under multiple laser lines throughout the visible–NIR spectral range. The effect of the polyvinylpyrrolidone coating on the SERS/SEF enhancement efficiency of the self-assembled nanoparticle films was investigated. By choosing Nile Blue A and Rhodamine 800 molecular chromophores as spectroscopic probes, the efficacy of the developed plasmonic films both as SEF and SERS substrates was demonstrated in a single measurement under visible (633 nm) and NIR (785 nm) laser excitation. Important to note is that the tested fluorophores could be detected based on their SERS fingerprint bands, even under conditions for fluorescence excitation and despite the PVP coating. Further research is necessary in order to optimize the thickness of the PVP layer needed to properly adjust the interplay between SERS and SEF as required by a specific configuration and parameters of target sensing application. The applicability of the proposed substrates for the detection of biologically relevant molecules was demonstrated by testing their SERS efficiency for the detection of metanephrine, a metabolite currently used for the biochemical diagnosis of neuroendocrine tumours. Although the utilization of SERS for the determination of neurotransmitters in practice is currently in the initial stage of study, primarily because these analytes do not have functional groups that could serve as anchors to the noble metal nanoparticle surface, we were able to detect the analyte at concentration levels similar to those previously reported for other catecholamine metabolites. For reaching lower concentrations and improving the reliability and robustness of future SERS-based metanephrine assays, surface functionalization schemes ought to be developed for an efficient and specific analyte trapping close to the metal surface. Our results also demonstrate that, by using a simple assembly method from easy-to-synthesize colloidal gold nanoparticles, an efficient substrate with a dual detection capability (SERS/SEF) can be obtained which might have a broader impact on the development of analytical application tools.

Author contributions

Conceptualization: C.F.; formal analysis: A.F. and C.F.; funding acquisition: C.F.; resources: S.B. and C.F.; investigation: all authors; methodology: all authors; visualization: A.-S.T., S.B., A.F., and C.F.; writing – original draft: all authors.

Conflicts of interest

There are no conflicts to declare.

Acknowledgements

References

1 R. P. M. Höller, I. J. Jahn, D. Cialla-May, M. Chanana, J. Popp, A. Fery and C. Kuttner, *ACS Appl. Mater. Interfaces*, 2020, **12**, 57302–57313.

2 A. Sultangaziyev and R. Bukasov, *Sens Biosensing Res*, 2020, **30**, 100382.

3 T. Lin, Y.-L. Song, J. Liao, F. Liu and T.-T. Zeng, *Nanomedicine*, 2020, **15**, 2971–2989.

4 J. Wu, L. Zhang, F. Huang, X. Ji, H. Dai and W. Wu, *J. Hazard. Mater.*, 2020, **387**, 121714.

5 K. Ge, Y. Hu and G. Li, *Biosensors*, 2022, **12**, 941.

6 L. Lu, J. Zhang, L. Jiao and Y. Guan, *Nanomaterials*, 2019, **9**, 916.

7 L. Lu, S. Guan, Y. Guan and M. Hong, *Adv. Mater. Interfaces*, 2022, **9**, 2102532.

8 J. Tang, H. Guo, M. Chen, J. Yang, D. Tsoukalas, B. Zhang, J. Liu, C. Xue and W. Zhang, *Sens. Actuators, B*, 2015, **218**, 145–151.

9 J. Tang, H. F. Wen, P. L. Chai, J. Liu, Y. B. Shi and C. Y. Xue, *J. Nano Res.*, 2012, **20**, 33–41.

10 S. Chang, S. L. Eichmann, T.-Y. S. Huang, W. Yun and W. Wang, *J. Phys. Chem. C*, 2017, **121**, 8070–8076.

11 I. Marica, M. Stefan, S. Boca, A. Falamaş and C. Farcău, *J. Colloid Interface Sci.*, 2023, **635**, 117–127.

12 D. Mampallil and H. B. Eral, *Adv. Colloid Interface Sci.*, 2018, **252**, 38–54.

13 Z. Yuan, D. B. Burckel, P. Atanassov and H. Fan, *J. Mater. Chem.*, 2006, **16**, 4637.

14 C. Farcau, M. Potara, C. Leordean, S. Boca and S. Astilean, *Analyst*, 2013, **138**, 546–552.

15 C. Yi, Y. Yang, B. Liu, J. He and Z. Nie, *Chem. Soc. Rev.*, 2020, **49**, 465–508.

16 V. Buhler, *Polyvinylpyrrolidone Excipients for Pharmaceuticals*, Springer-Verlag, Berlin/Heidelberg, 2005.

17 A. Göthlich, S. Koltzenburg and G. Schornick, *Chem. Unserer Zeit*, 2005, **39**, 262–273.

18 F. Fischer and S. Bauer, *Chem. Unserer Zeit*, 2009, **43**, 376–383.

19 B.-H. Sohn, J.-M. Choi, S. I. Yoo, S.-H. Yun, W.-C. Zin, J. C. Jung, M. Kanehara, T. Hirata and T. Teranishi, *J. Am. Chem. Soc.*, 2003, **125**, 6368–6369.

20 K. M. Koczkur, S. Mourdikoudis, L. Polavarapu and S. E. Skrabalak, *Dalton Trans.*, 2015, **44**, 17883–17905.

21 T. Nagy-Simon, A.-S. Tatar, A.-M. Craciun, A. Vulpoi, M.-A. Jurj, A. Florea, C. Tomuleasa, I. Berindan-Neagoe, S. Astilean and S. Boca, *ACS Appl. Mater. Interfaces*, 2017, **9**(25), 21155–21168.

22 M. Urbieta, M. Barbry, Y. Zhang, P. Koval, D. Sánchez-Portal, N. Zabala and J. Aizpurua, *ACS Nano*, 2018, **12**, 585–595.

23 H. Yuan, C. G. Khoury, H. Hwang, C. M. Wilson, G. A. Grant and T. Vo-Dinh, *Nanotechnology*, 2012, **23**, 075102.

24 N. Gupta, A. Ninawe and A. Dhawan, in *Plasmonics in Biology and Medicine XVII*, ed. T. Vo-Dinh, H.-P. A. Ho and K. Ray, SPIE, San Francisco, United States, 2020, p. 8.

25 T. Chung and S.-H. Lee, *Plasmonics*, 2022, **17**, 2113–2121.

26 S. Zhu and M. Cortie, *Proc. SPIE*, 2015, **9668**, 96683R.

27 S. K. Dondapati, T. K. Sau, C. Hrelescu, T. A. Klar, F. D. Stefani and J. Feldmann, *ACS Nano*, 2010, **4**, 6318–6322.

28 A.-S. Tatar, C. Farcău, A. Vulpoi, S. Boca and S. Astilean, *Spectrochim. Acta, Part A*, 2022, **273**, 121069.

29 V. Shvalya, G. Filipič, J. Zavašnik, I. Abdulhalim and U. Cvelbar, *Appl. Phys. Rev.*, 2020, **7**, 031307.

30 V. S. Gummaluri, R. Gayathri, C. Vijayan and V. M. Murukeshan, *J. Opt.*, 2020, **22**, 065003.

31 Le Peng, Lu Zhou, Y.-ping Qing, Li.-ying Tong, Z.-heng Liang, H. Fu and J. Zhou, *Acta Photonica Sin.*, 2020, **49**, 817002–817002.

32 Y. Li, J. Sun, L. Wu, J. Ji, X. Sun and Y. Qian, *Biosens. Bioelectron.*, 2014, **62**, 255–260.

33 G. Barbillon, O. Graniel and M. Bechelany, *Nanomaterials*, 2021, **11**, 2174.

34 Y. M. Sabri, A. E. Kandjani, S. J. Ippolito and S. K. Bhargava, *Sci. Rep.*, 2016, **6**, 24625.

35 S. Picciolini, N. Castagnetti, R. Vanna, D. Mehn, M. Bedoni, F. Gramatica, M. Villani, D. Calestani, M. Pavesi, L. Lazzarini, A. Zappettini and C. Morasso, *RSC Adv.*, 2015, **5**, 93644–93651.

36 Q. Mao, W. Jing, W. Gao, Z. Wei, B. Tian, M. Liu, W. Ren and Z. Jiang, *Micromachines*, 2021, **12**, 977.

37 A.-S. Tatar, A. Jurj, C. Tomuleasa, A. Florea, I. Berindan-Neagoe, D. Cialla-May, J. Popp, S. Astilean and S. Boca, *Colloids Surf., B*, 2019, **184**, 110478.

38 J. Turkevich, P. C. Stevenson and J. Hillier, *Discuss. Faraday Soc.*, 1951, **11**, 55.

39 G. Frens, *Nat. Phys. Sci.*, 1973, **241**, 20–22.

40 L. Gharibshahi, E. Saion, E. Gharibshahi, A. H. Shaari and K. A. Matori, *PLoS One*, 2017, **12**, e0186094.

41 C. Farcau, N. M. Sangeetha, N. Decorde, S. Astilean and L. Ressier, *Nanoscale*, 2012, **4**, 7870–7877.

42 A. Kedia, R. Singhal and P. Senthil Kumar, *Chem. Phys. Lett.*, 2022, **807**, 140101.

43 S. S. B. Moram, C. Byram and V. R. Soma, *Bull. Mater. Sci.*, 2020, **43**, 53.

44 E. Fort and S. Grésillon, *J. Phys. D: Appl. Phys.*, 2008, **41**, 013001.

45 S. Boca, C. Farcau, M. Baia and S. Astilean, *Biomed. Microdevices*, 2016, **18**, 12.

46 O. E. Eremina, N. R. Yarenkov, O. O. Kapitanova, A. S. Zelenetskaya, E. A. Smirnov, T. N. Shekhovtsova, E. A. Goodilin and I. A. Veselova, *Microchim. Acta*, 2022, **189**, 211.

47 A. Hariharan and P. Vadlamudi, *J. Mol. Struct.*, 2021, **1246**, 131163.